



**CHARACTERIZATION OF NICKEL
OXIDE QUANTUM DOTS AS HOLE
TRANSPORT MATERIAL IN
PEROVSKITE SOLAR CELLS**

SUBATHRA A/P MUNIANDY

**MASTER OF SCIENCE
IN ELECTRONIC ENGINEERING**

2024



Faculty of Electronics and Computer Technology and Engineering

CHARACTERIZATION OF NICKEL OXIDE QUANTUM DOTS AS HOLE TRANSPORT MATERIAL IN PEROVSKITE SOLAR CELLS

Subathra A/P Muniandy

Master of Science in Electronic Engineering

2024

**CHARACTERIZATION OF NICKEL OXIDE QUANTUM DOTS AS HOLE
TRANSPORT MATERIAL IN PEROVSKITE SOLAR CELLS**

SUBATHRA A/P MUNIANDY

**A thesis submitted
in fulfillment of the requirements for the degree of Master of Science
in Electronic Engineering**

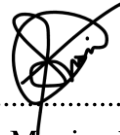
Faculty of Electronics and Computer Technology and Engineering

UNIVERSITI TEKNIKAL MALAYSIA MELAKA

2024

DECLARATION

I declare that this thesis entitled “Characterization of Nickel Oxide Quantum Dots as Hole Transport Material in Perovskite Solar Cells” is the result of my own research except as cited in the references. The thesis has not been accepted for any degree and is not concurrently submitted in candidature of any other degree.

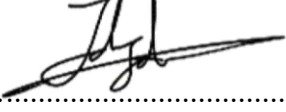


Signature :
Name :
Subathra Muniandy
Date :
03/01/2024

APPROVAL

I hereby declare that I have read this thesis and in my opinion this thesis is sufficient in terms of scope and quality for the award of Master of Science in Electronic Engineering.

Signature

:.....


Supervisor Name

Dr. Muhammad Idzdihar Bin Idris
:.....

Date

19/01/2024
:.....

DEDICATION

This research paper is sincerely dedicated to my beloved mother and father who encouraged and inspired me in conducting this study. They have never left my side and gave me strength and hope throughout my study. They provide me with a great sense of enthusiasm and perseverance in continuing this research work. Without their love and assistance, this research would not have been made possible. Moreover, I dedicate this research paper to my research supervisor, Dr. Muhammad Idzdihar Bin Idris, and co-supervisor, Dr. Zul Atfyi Fauzan Bin Mohammed Napiah, who constantly provides guidance and support. I could not have undertaken this journey without them, who generously provided knowledge and expertise. Additionally, this research work endeavor would not have been possible without the generous support from Universiti Teknikal Malaysia Melaka (UTeM) for grant funding for the financial support throughout this project. I am also grateful to my friends, for their editing help, feedback sessions, and moral support. Lastly, I thanked Almighty God who gave me strength, wisdom, guidance, power of thinking, security, and competence and for giving me good health while doing this research work.

ABSTRACT

Perovskite solar cells (PSCs) have attracted the interest of researchers owing to their excellent light absorption, improved carrier mobility, high-power conversion efficiency and sustainable photovoltaic cell. PSCs have charge transport materials known as electron transporting layers (ETL) and hole transporting layers (HTL) that interact with the perovskite layer. The HTL is a fundamental component in PSC structures which are generally composed of a Spiro-OMeTAD and PEDOT:PSS material that has a drawback of a high cost, lengthy synthesis process, and insufficient long-term stability. Nickel oxide (NiO) as an inorganic HTL has been emphasized in PSCs owing to low cost, solution-based processing and the good band alignment as HTL in PSCs. Despite the extensive investigation of NiO, the importance of altering the pH of the precursor solution to improve the performance of HTL remains significant which have impact on the morphologies, crystal sizes, and textural qualities of the material. This project proposes a novel idea for introducing NiO quantum dots (QDs) in the HTL to achieve high efficiency and flexibility. The experimental study present the effect of the bottom and top layer of synthesized NiO at different pH values (9-12) using a spin-coating method annealed at 500 °C, 600 °C, and 700 °C. The in-depth characterization of the synthesized NiO was executed by XRD, UV-Vis spectroscopy, FTIR, AFM, SEM, TEM, PL, RF Impedance Analyzer, and four point-probe to investigate their structural, optical, element composition, surface roughness, morphological, quantum size, optical emission, dielectric constant, and resistivity properties. The performance of full fabricated PSC based on NiO or PEDOT:PSS/MAPbI₃/Graphene/ZnO/Ag were evaluated by current-voltage (I-V) curve. According to XRD findings, all the prominent diffraction peaks of NiO at 37.2°, 43.36°, 63.04°, and 75.51° were observed only in pH 11 at both layers. The SEM revealed the surface morphology of pH 11 have good coverage with less agglomeration of particles as compared to other pH values. The absorption spectrum of pH 11 was noticed in the UV region with band gap increasing from 3.45 to 3.64 for bottom layer and 3.42 to 3.47 for top layer. This research confirmed the quantum confinement effect obtained at pH 11 NiO through the reduction of crystallite size with higher bandgap energy. The impedance analyzer implies the layers of pH 11 NiO (700 °C) have higher dielectric constant (7.09 for bottom layer and 7.20 for top layer) with minimal polarization effect. A strong absorption peak were observed in FTIR analysis (400cm⁻¹ to 600cm⁻¹), ascribed to the presence of NiO vibration. TEM analysis revealed an average particle size of about 9.82 nm and 10.6 nm for the bottom and top layer of pH 11 NiO respectively. The observation of blue shifted PL emission bands that extended from 532 nm to 550 nm into the visible area proved that pH 11 NiO has high charge transfer resistance. The inverted PSC fabricated with bottom and top layer pH 11 NiO (700 °C) showed better performance than for the inverted PSC based on PEDOT:PSS. Based on these findings, NiO produced at pH 11 annealed at 700 °C exhibited promising characteristics, suitable for HTL in PSCs.

PENCIRIAN BINTIK KUANTUM NIKEL OKSIDA SEBAGAI BAHAN PENGANGKUTAN LUBANG DALAM SEL SURIA PEROVSKIT

ABSTRAK

Sel suria perovskit telah menarik minat penyelidik kerana penyerapan cahaya yang sangat baik, mobiliti pembawa yang lebih baik, kecekapan penukaran kuasa tinggi dan sel fotovoltaik yang mampan. PSC mempunyai bahan pengangkutan cas yang dikenali sebagai lapisan pengangkut elektron dan lapisan pengangkut lubang yang berinteraksi dengan lapisan perovskit. HTL ialah komponen asas dalam struktur PSC yang umumnya terdiri daripada bahan Spiro-OMeTAD dan PEDOT:PSS yang mempunyai kelemahan kos yang tinggi, proses sintesis yang panjang dan kestabilan jangka panjang yang tidak mencukupi. Nikel oksida (NiO) sebagai HTL tak organik telah ditekankan dalam PSC kerana kos rendah, pemprosesan berasaskan penyelesaian dan penajaran jalur yang baik sebagai HTL dalam PSC. Walaupun penyiasatan meluas NiO , kepentingan mengubah pH larutan prekursor untuk meningkatkan prestasi HTL kekal penting yang mempunyai kesan ke atas morfologi, saiz kristal dan kualiti tekstur bahan. Projek ini mencadangkan idea baru untuk memperkenalkan bintik kuantum NiO dalam HTL untuk mencapai kecekapan dan fleksibiliti yang tinggi. Kajian eksperimen membentangkan kesan lapisan bawah dan atas NiO tersintesis pada nilai pH yang berbeza (9-12) menggunakan kaedah salutan putaran disepuh pada $500\text{ }^{\circ}\text{C}$, $600\text{ }^{\circ}\text{C}$ dan $700\text{ }^{\circ}\text{C}$. Pencirian mendalam NiO yang disintesis telah dilaksanakan oleh XRD, spektroskopi UV-Vis, FTIR, AFM, SEM, TEM, PL, Penganalisis Impedans RF, dan pengesan empat bintik untuk menyiasat struktur, optik, komposisi unsur, kekasaran permukaannya, morfologi, saiz kuantum, pelepasan optik, pemalar dielektrik, dan sifat kerintangan. Prestasi PSC fabrikasi penuh berdasarkan NiO atau PEDOT:PSS/MAPbI₃/Grapene/ZnO/Ag telah dinilai oleh lengkung voltan semasa (I-V). Menurut penemuan XRD, semua puncak pembelauan ketara NiO pada 37.2° , 43.36° , 63.04° , dan 75.51° hanya diperhatikan dalam pH 11 pada kedua-dua lapisan. SEM mendedahkan morfologi permukaan pH 11 mempunyai liputan yang baik dengan kurang aglomerasi zarah berbanding dengan nilai pH lain. Spektrum penyerapan pH 11 telah diperhatikan di kawasan UV dengan jurang jalur meningkat daripada 3.45 kepada 3.64 untuk lapisan bawah dan 3.42 hingga 3.47 untuk lapisan atas. Penyelidikan ini mengesahkan kesan kurungan kuantum yang diperoleh pada pH 11 NiO melalui pengurangan saiz kristal dengan tenaga celah jalur yang lebih tinggi. Penganalisis impedans membayangkan lapisan pH 11 NiO ($700\text{ }^{\circ}\text{C}$) mempunyai pemalar dielektrik yang lebih tinggi (7.09 untuk lapisan bawah dan 7.20 untuk lapisan atas) dengan kesan polarisasi yang minimum. Puncak penyerapan yang kuat telah diperhatikan dalam analisis FTIR (400cm^{-1} hingga 600cm^{-1}), dikaitkan dengan kehadiran getaran NiO . Analisis TEM mendedahkan saiz zarah purata kira-kira 9.82 nm dan 10.6 nm untuk lapisan bawah dan atas pH 11 NiO masing-masing. Pemerhatian jalur pelepasan PL anjakan biru yang memanjang dari 532 nm hingga 550 nm ke kawasan yang boleh dilihat membuktikan bahawa pH 11 NiO mempunyai rintangan pemindahan cas yang tinggi. PSC terbalik yang direka dengan lapisan bawah dan atas pH 11 NiO ($700\text{ }^{\circ}\text{C}$) menunjukkan prestasi yang lebih baik daripada PSC terbalik berdasarkan PEDOT:PSS. Berdasarkan penemuan ini, NiO yang dihasilkan pada pH 11 anil pada $700\text{ }^{\circ}\text{C}$ memamerkan ciri-ciri yang menjanjikan, sesuai untuk HTL dalam PSC.

ACKNOWLEDGEMENTS

First and foremost, I would like to take this opportunity to express my sincere acknowledgment to my supervisor Dr. Muhammad Idzdihar Bin Idris from the Faculty of Electronics and Computer Technology and Engineering Universiti Teknikal Malaysia Melaka (UTeM) for his essential supervision, support, and encouragement towards the completion of this thesis.

I would also like to express my greatest gratitude to Dr. Zul Atfyi Fauzan Bin Mohammed Napiah from the Faculty of Electronics and Computer Technology and Engineering, co-supervisor of this project for his advice and suggestions. Special thanks to UTeM for short-term grant funding for the financial support throughout this project. Additionally, this endeavor would not have been possible without the generous support from the Nano-Optoelectronics Research & Technology Laboratory (NOR Lab), School of Physics, Universiti Sains Malaysia (USM) and Functional Nanotechnology Device Laboratory, Institute of Nanoscience and Nanotechnology (ION2), Universiti Putra Malaysia (UPM) for the technical equipment used in my research.

Particularly, I would also like to express my deepest gratitude to Mr. Wahyudi, the technician from the Faculty of Electrical Technology and Engineering, Mr. Hairul Hisham, the technician from the material laboratory Faculty of Industrial and Manufacturing Technology and Engineering, Mr. Mahader the technician from the Faculty of Mechanical Technology and Engineering. Mr. Azmi, and Mr. Sufian, technicians from MiNe and microwave laboratory Faculty of Electronics and Computer Technology and Engineering, for their assistance and efforts in all the lab and analysis works.

Special thanks to all my peers, my mother, my beloved father, and my siblings for their moral support in completing this master's study. Lastly, thank you to everyone who had been to the crucial parts of the realization of this project.

TABLE OF CONTENTS

	PAGE
DECLARATION	
APPROVAL	
DEDICATION	
ABSTRACT	i
ABSTRAK	ii
ACKNOWLEDGEMENTS	iii
TABLE OF CONTENTS	iv
LIST OF TABLES	vii
LIST OF FIGURES	viii
LIST OF ABBREVIATIONS	xv
LIST OF SYMBOLS	xx
LIST OF PUBLICATIONS	xxi
 CHAPTER	
1. INTRODUCTION	1
1.0 Background of Study	1
1.1 Problem Statement	2
1.2 Research Objectives	4
1.3 Research Scope of Work	5
1.4 Research Contribution	6
1.5 Thesis Outline	7
2. LITERATURE REVIEW	9
2.0 Renewable Energy Sources	9
2.1 Solar Energy	11
2.2 Photovoltaic (PV)	13
2.2.1 First Generation	14
2.2.2 Second Generation	15
2.2.3 Third Generation	16
2.3 Perovskite Solar Cells (PSCs)	18
2.3.1 Role of Perovskite	18
2.3.2 Types of Structure	19
2.3.3 Methylammonium lead iodide (MAPbI_3)	20
2.3.4 Electron Transporting Material (ETM)	22
2.3.4.1 Zinc Oxide (ZnO)	24
2.3.4.2 Passivation interlayer as Graphene polymer	25
2.3.5 Hole Transporting Material (HTM)	28
2.3.5.1 Small molecules	29
2.3.5.2 Polymer	30
2.3.5.3 In-organic material	31
2.4 Nickel Oxide (NiO)	34
2.4.1 Recent development of NiO as HTL	35
2.5 Quantum Dots (QDs)	56
2.6 Quantum Confinement	57
2.7 Photovoltaic performance metrics	58
2.7.1 Power conversion efficiency (PCE)	58
2.7.2 Open-Circuit Voltage (V_{oc})	59

2.7.3	Short-Circuit Current Density (J_{SC})	60
2.7.4	Fill Factor (FF)	61
2.8	Summary	62
3.	MATERIALS AND METHODS/METHODOLOGY	64
3.0	Experimental Material	64
3.1	Experimental Procedure	65
3.1.1	Substrate preparation	66
3.1.2	Synthesis of NiO	66
3.1.3	Synthesis of MAPbI_3	68
3.1.4	Synthesis of ZnO and Graphene Binder	69
3.1.5	Deposition of NiO thin film	70
3.1.6	Fabrication of PSCs	72
3.2	Material Characterizations	77
3.2.1	Solar Simulator for I-V measurement	78
3.3	Summary	80
4.	RESULT AND DISCUSSION	82
4.0	Characterization of NiO thin film for different pH (9 – 12)	82
4.1	Structural Analysis	83
4.1.1	pH 9 of NiO	84
4.1.2	pH 10 of NiO	89
4.1.3	pH 11 of NiO	93
4.1.4	pH 12 of NiO	99
4.2	Morphological Analysis	103
4.2.1	pH 9 of NiO	105
4.2.2	pH 10 of NiO	106
4.2.3	pH 11 of NiO	106
4.2.4	pH 12 of NiO	107
4.3	Optical Analysis	108
4.3.1	pH 9 of NiO	109
4.3.2	pH 10 of NiO	111
4.3.3	pH 11 of NiO	113
4.3.4	pH 12 of NiO	115
4.4	Dielectric Constant	120
4.4.1	pH 9 of NiO	121
4.4.2	pH 10 of NiO	123
4.4.3	pH 11 of NiO	125
4.4.4	pH 12 of NiO	127
4.5	Element composition of NiO	130
4.6	Surface roughness of NiO	132
4.7	Quantum Dots of NiO	136
4.8	Photoluminescent (PL) of NiO	138
4.9	Characterization of MAPbI_3 and ZnO thin film	141
4.9.1	Characterization of Methylammonium Lead Iodide (MAPbI_3) thin film	141
4.9.1.1	Structural Analysis of MAPbI_3	141
4.9.1.2	Morphology Analysis of MAPbI_3	142
4.9.1.3	Optical Analysis of MAPbI_3	143

4.9.2	Characterization of ZnO thin film	144
4.9.2.1	Structural Analysis of ZnO	144
4.9.2.2	Morphology Analysis of ZnO	145
4.9.2.3	Optical Analysis of ZnO	146
4.10	Characterization of NiO (bottom and top)/MAPbI ₃ thin film	147
4.10.1	Structural Analysis of NiO(bottom and top)/MAPbI ₃	147
4.10.2	Morphology Analysis of NiO(bottom and top)/MAPbI ₃	149
4.10.3	Optical Analysis of NiO(bottom and top)/MAPbI ₃	150
4.11	Characterization of (wet and dry) ZnO/MAPbI ₃ and ZnO/ Graphene/ MAPbI ₃ thin film	151
4.11.1	Structural Analysis of (wet and dry) ZnO/MAPbI ₃	152
4.11.2	Morphology Analysis of (wet and dry) ZnO/MAPbI ₃	153
4.11.3	Optical Analysis of (wet and dry) ZnO/MAPbI ₃	154
4.11.4	Structural Analysis of HIA (ZnO/Graphene/MAPbI ₃)	157
4.11.5	Morphology Analysis of HIA (ZnO/Graphene/MAPbI ₃)	158
4.11.6	Optical Analysis of HIA (ZnO/Graphene/MAPbI ₃)	159
4.12	Characterization of Solar Cell (I-V) curve	160
4.13	Summary	171
5.	CONCLUSION AND RECOMMENDATIONS FOR FUTURE RESEARCH	172
5.0	Conclusion	172
5.1	Recommendation	174
6.	REFERENCE	176

LIST OF TABLES

TABLE	TITLE	PAGE
2.1	Summary of NiO thin films as HTL in PSCs with different parameters	41
3.1	Analytical characterization techniques and evaluated parameters for NiO thin films in PSCs	78
4.1	The structural properties of the bottom and top layer NiO thin film at pH 9 with different annealing temperatures	89
4.2	The structural properties of the bottom and top layer NiO thin film at pH 10 with different annealing temperatures	92
4.3	The structural properties of the bottom and top layer NiO thin film at pH 11 with different annealing temperatures	99
4.4	The structural properties of the bottom and top layer NiO thin film at pH 12 with different annealing temperatures	103
4.5	The energy bandgap of the bottom and top layer NiO thin film at a different pH value	119
4.6	The dielectric constant of the bottom and top layer NiO thin film at different pH value	129
4.7	The comparative result of photovoltaic performance analysis of various PSCs configurations with different HTLs (NiO and PEDOT:PSS)	168
4.8	An analysis comparing crystalline size, pH level, surface morphology, quantum dots, energy bandgap, and photovoltaic performance across previous and current research.	169

LIST OF FIGURES

FIGURE	TITLE	PAGE
2.1	Types of renewable energy and their application (Rowley and Westwood, 2015)	10
2.2	Renewable power capacity growth (Renewable Energy Agency, 2020)	11
2.3	Illustration of the Earth's atmosphere's energy balances involving receiving Sun energy and releasing Earth energy (Effiong and Neitzel, 2016)	12
2.4	Different generations of solar cells (Ibn-Mohammed, Taofeq, Koh et al., 2017)	14
2.5	1 st generation of bulk silicon	15
2.6	2 nd generation of flexible amorphous thin film	16
2.7	3 rd generation of (a) QD s solar cell and (b) solid-state of DSSC	17
2.8	Band diagram and operation principle of perovskite solar cell (Marinova, Valero and Delgado, 2017)	19
2.9	Generic structures of (a) conventional (n-i-p), (b) inverted planar (p-i-n) and, (c) mesoporous (conventional) perovskite solar cells (Hussain et al., 2018)	20
2.10	The crystal structure of MAPbI ₃	21
2.11	Energy levels of various materials operating as inorganic ETMs in planar system configuration (Hussain et al., 2018)	23
2.12	Stick and ball representation of ZnO crystal structures: (a) cubic rocksalt, (b) cubic zincblende, and (c) hexagonal wurtzite	25
2.13	Chemical structure of graphene	27
2.14	Schematic illustration of principle defects in a typical MAPbI ₃ perovskite structure	28
2.15	Energy levels of various materials working as HTM in planar system configuration (Hussain et al., 2018)	29
2.16	The crystal structures of NiO, in which Ni ²⁺ and O ²⁻ ions consecutively form to create NiO (Diao et al., 2020)	35
2.17	The influence of particle size on the bandgap and splitting of energy levels due to the quantum confinement effect (Mansur, 2010)	58
2.18	A plot depicting the current output of the cell (represented by the	62

red line) and the power output (depicted by the blue line) relative to voltage.	
3.1 Overall flowchart of the experimental procedure	65
3.2 The detailed synthesis of the NiO procedure	67
3.3 Flow chart of synthesis of NiO	68
3.4 Schematic diagram of (a) preparation of PbI ₂ and (b) preparation of MAI	69
3.5 Illustration of (a) binder preparation, (b) ZnO nanoparticles mixed with a binder, and (c) Graphene mixed with a binder	70
3.6 Diagram of NiO deposition process repeated for 10 cycle and annealed at three different temperature	71
3.7 Flow chart of deposition process and material characterization of NiO	72
3.8 (a) Kapton tape used to cover the surface of the glass plate to the bench top, bottom and sides. (b) Schematic drawing of the full fabrication process of inverted PSCs. (c) The outcome of the sample in each step and the final view of a 3 by 3 array of inverted PSCs.	75
3.9 Schematic layout of the inverted PSCs studied in the present work, along with the respective thickness of each layer.	76
3.10 Solar simulator with Keithley's Model 2459 Interactive source meter	79
3.11 Schematic of the close-up look for the current-voltage (I-V) measurement	80
4.1 X-ray diffraction patterns of pH 9 NiO film at (a) as-deposited bottom layer, (b) different temperature of the bottom layer, (c) as-deposited top layer, and (d) different temperature of the top layer.	87
4.2 The WH analysis for the bottom layer NiO thin film at pH 9 showed the positive strain at (a) 500°C, and (b) 700°C. Solid lines represent best-fitting lines, while error bars represent standard deviations. The slope was used to determine the strain, and the y-intercept was used to calculate the crystalline size.	88
4.3 The WH analysis for the top layer NiO thin film at pH 9 (a) 500°C, and (b) 600°C. Solid lines represent best-fitting lines, while error bars represent standard deviations.	88

4.4	X-ray diffraction patterns for pH value of 10 NiO film at (a) as-deposited bottom layer, (b) different temperature of the bottom layer, (c) as-deposited top layer, and (d) different temperature of the top layer.	91
4.5	The WH analysis for the bottom layer NiO thin film of pH 10 annealed at 600°C. Solid lines represent best-fitting lines, while error bars represent standard deviations obtained from Origin software.	92
4.6	X-ray diffraction patterns of pH 11 NiO film at (a) as-deposited bottom layer, (b) different temperature of bottom layer, (c) as- deposited top layer, and (d) different temperature of top layer.	96
4.7	The W-H analysis for the bottom layer NiO thin film at pH 11 (a) as-deposited (b)500 °C, (c) 600 °C and (d) 700°C. Solid lines represent best-fitting lines, while error bars represent standard deviations.	97
4.8	The W-H analysis for the top layer NiO thin film at pH 11 (a) as-deposited, (b)500 °C, (c)600°C and (d) 700°C. Solid lines represent best-fitting lines, while error bars represent standard deviations.	98
4.9	X-ray diffraction patterns of pH 12 NiO film at (a) as-deposited bottom layer, (b) different temperature of the bottom layer, (c) as-deposited top layer, and (d) different temperature of the top layer.	101
4.10	The W-H analysis for the bottom layer NiO thin film at pH 12 (a)500 °C, (b)600°C and (c) 700°C. Solid lines represent best-fitting lines, while error bars represent standard deviations.	102
4.11	NiO thin films' colour changing before and after annealing at 500°C, 600°C and 700°C for (a) the bottom layer and (b) the top layer.	104
4.12	The SEM images of NiO thin films at pH 9 as-deposited and annealed sample (500°C, 600°C and 700°C) for (a) bottom layer and (b) top layer	105
4.13	The SEM images of NiO thin films at pH 10 as-deposited and annealed sample (500°C, 600°C and 700°C) for	106

	(a) bottom layer and (b) top layer	
4.14	The SEM images of NiO thin films at pH 11 as-deposited and annealed sample (500°C, 600°C and 700°C) for (a) bottom layer and (b) top layer	107
4.15	The SEM images of NiO thin films at pH 12 as-deposited and annealed sample (500°C, 600°C and 700°C) for (a) bottom layer and (b) top layer	108
4.16	UV-Vis spectrum of NiO thin films at pH 9 for as-deposited and with different annealing temperatures (a) absorption spectra of the bottom layer, (b) Tauc plot of bottom layer, (c) absorption spectra of the top layer and (d) Tauc plot of the top layer	111
4.17	UV-Vis spectrum of NiO thin films at pH 10 for as-deposited and with different annealing temperatures (a) absorption spectra of the bottom layer, (b) Tauc plot of bottom layer, (c) absorption spectra of the top layer and (d) Tauc plot of the top layer	112
4.18	UV-Vis spectrum of NiO thin films at pH 11 for as-deposited and with different annealing temperatures (a) absorption spectra of the bottom layer, (b) Tauc plot of bottom layer, (c) absorption spectra of the top layer and (d) Tauc plot of the top layer	114
4.19	UV-Vis spectrum of NiO thin films at pH 12 for as-deposited and with different annealing temperatures (a) absorption spectra of the bottom layer, (b) Tauc plot of bottom layer, (c) absorption spectra of the top layer and (d) Tauc plot of the top layer	116
4.20	The comparison of energy bandgap values derived from the Tauc plot made across four different pH levels for both bottom and top layer NiO as-deposited and annealed sample.	118
4.21	The frequency dependence of dielectric constant of pH 9 for as-deposited and different annealing temperatures of the NiO film at the (a) bottom layer, (b) top layer, (c) dielectric loss tangent of the bottom layer and (d) dielectric loss tangent of the top layer	122
4.22	The frequency dependence of dielectric constant of pH 10 for as-deposited and different annealing temperatures of the NiO film at the (a) bottom layer, (b) top layer, (c) dielectric loss tangent of the bottom layer and (d) dielectric loss tangent of the top layer	124
4.23	The frequency dependence of dielectric constant of pH 11 for	126

	as-deposited and different annealing temperatures of the NiO film at the (a) bottom layer, (b) top layer, (c) dielectric loss tangent of the bottom layer and (d) dielectric loss tangent of the top layer	
4.24	The frequency dependence of dielectric constant of pH 12 for as-deposited and different annealing temperatures of the NiO film at the (a) bottom layer, (b) top layer, (c) dielectric loss tangent of the bottom layer and (d) dielectric loss tangent of the top layer	128
4.25	FTIR spectrum of the NiO film at a different pH value (9 -12)	131
4.26	AFM topographic images obtained at height sensor of (10 μ m) for bottom layer pH 11 NiO thin film (a) as-deposited, (b) 500 °C, (c) 600 °C and (d) 700 °C	135
4.27	AFM topographic images obtained at height sensor of (10 μ m) for top layer pH 11 NiO thin film (a) as-deposited, (b) 500 °C, (c) 600 °C and (d) 700 °C	135
4.28	TEM micrographs of the pH 11 NiO for (a) bottom layer, (b) top layer, (c) particle size distribution of bottom layer and (d) particle size distribution of top layer	137
4.29	EDS spectrum of the pH 11 NiO at 700 °C (a) bottom layer, and (b) top layer	138
4.30	(a) The comparison of PL emission spectra for bottom and top layer pH 11 NiO excited at 365 nm and 405 nm, revealing deep-level emission extending to the visible region; (b) demonstrating various PL emission components that originated due to electronic transition between different defect levels and band edge of NiO	140
4.31	The XRD patterns of MAPbI ₃ perovskite thin films, including PbI ₂ peaks obtained after 10 minutes of annealing at 100°C	142
4.32	The top view of SEM morphology of (a) MAPbI ₃ perovskite thin films with the colour change of the MAPbI ₃ observed after 6 days and (b) grain size distribution of MAPbI ₃ perovskite thin films along with the degradation behaviour of the thin film after 6 days	143
4.33	(a) UV–Vis absorbance spectra of MAPbI ₃ thin films and (b) energy bandgap of MAPbI ₃ using the Tauc formula (Muniandy et al., 2022)	144
4.34	The XRD patterns of ZnO thin films	145

4.35	The top view of SEM morphology of (a) ZnO thin films at 5K magnification, (b) ZnO thin films at 20K magnification along with surface appearance of ZnO and (c) grain size distribution of ZnO thin films	146
4.36	(a) UV–Vis absorbance spectra of ZnO thin films and (b) energy bandgap of ZnO thin films using Tauc formula	147
4.37	XRD patterns of MAPbI ₃ films grown on (a) bottom-NiO (700°C) and (b) top-NiO (700°C). No presence PbI ₂ peaks in both layer however, the more prominent peak was observed in NiO/MAPbI ₃ (bottom)	148
4.38	Top view SEM images of MAPbI ₃ films grown on the surface of (a) bottom NiO (700°C), (b) top-NiO (700°C), (c) grain size distribution of bottom NiO/ MAPbI ₃ and (d) grain size distribution of top NiO/ MAPbI ₃ along with the surface appearance of thin film	149
4.39	UV–vis absorbance spectra of MAPbI ₃ films on (a) bottom and top NiO (700°C), and (b) Tauc plot of bottom NiO/ MAPbI ₃ and top NiO/ MAPbI ₃	151
4.40	XRD spectrum of MAPbI ₃ films grown on (a) wet-ZnO and (b) dry-ZnO	153
4.41	Top view SEM images of MAPbI ₃ films grown on the surface of (a) dry-ZnO, (b) wet-ZnO, and (c) grain size distribution of wet-ZnO/MAPbI ₃ along with the decomposition behavior of thin film	154
4.42	UV–vis absorbance spectra of MAPbI ₃ films on (a) dry ZnO, (b) wet ZnO, and Tauc plot of bottom (c) dry-ZnO/MAPbI ₃ and (d) wet-ZnO/MAPbI ₃	155
4.43	Architecture of inverted PSCs, including graphene as a passivation layer	157
4.44	XRD patterns of ZnO/Graphene/MAPbI ₃ interface	158
4.45	Top view of SEM images illustrated on the right indicating the MAPbI ₃ films grown on the surface of ZnO/Graphene/MAPbI ₃ interface and displays clear discoloration after few days. The overview schematics diagram of the growth of perovskite deposited on (a) dry ZnO, (b) wet ZnO and (c) dry ZnO/graphene polymer are shown on the left	159
4.46	(a) UV–vis absorbance spectra of ZnO/Graphene/MAPbI ₃ interface	160

	and (b) the optical bandgap of ZnO/Graphene/MAPbI ₃ film determined by Tauc equation	
4.47	I-V curves of the inverted PSCs obtained from pH 11 bottom layer annealed at 700 °C (a) NiO/Ag, (b) NiO/MAPbI ₃ /Ag, (c) NiO/MAPbI ₃ /Graphene/Ag and (d) NiO/MAPbI ₃ /Graphene/ ZnO/Ag with corresponding photovoltaic parameters of solar cells	165
4.48	I-V curves of the inverted PSCs obtained from pH 11 top layer annealed at 700 °C (a) NiO/Ag, (b) NiO/MAPbI ₃ /Ag, (c) NiO/MAPbI ₃ /Graphene/Ag and (d) NiO/MAPbI ₃ /Graphene/ ZnO/Ag with corresponding photovoltaic parameters of solar cells	166
4.49	I-V curves of the inverted PSCs obtained from (a) PEDOT:PSS/Ag, (b) PEDOT:PSS/MAPbI ₃ /Ag, (c) PEDOT:PSS/MAPbI ₃ / Graphene/Ag and (d) PEDOT:PSS/MAPbI ₃ /Graphene/ZnO/Ag with corresponding photovoltaic parameters of solar cells	167

LIST OF ABBREVIATIONS

PV	-	Photovoltaic
Si	-	Silicon
c-Si	-	Crystalline silicon
a-Si	-	Amorphous silicon
PSCs	-	Perovskite solar cells
DSSC	-	Dye-sensitized solar cells
HTM	-	Hole transmission material
HTL	-	Hole transport layer
ETL	-	Electron transporting layer
ETM	-	Electron transport material
QDs	-	Quantum dots
IPCE	-	Incident photon to current conversion efficiency
GPVDM	-	General-Purpose Photovoltaic Device Mode
PCE	-	Power conversion efficiency
FF	-	Fill factor
XRD	-	X-ray diffraction spectrometer
SEM	-	Scanning electron microscope
UV-Vis	-	UV-visible spectroscopy
FTIR	-	Fourier-transform infrared spectroscopy
AFM	-	Atomic force microscope
TEM	-	Transmission electron microscopy
IRENA	-	International Renewable Energy Agency
PL	-	Photoluminescence
DC	-	Direct current
RMS	-	Root-mean-square
TCO	-	Transparent conductive oxide
OPV	-	Organic photovoltaic
JCPDS	-	Joint committee on powder diffraction standard
XPS	-	X-ray photoelectron spectroscopy
VB	-	Valence band
CB	-	Conduction band
SRH	-	Shockley-Read-Hall

HIA	-	Hybrid interfacial architecture
HOMO	-	Highest occupied molecular orbital
W-H	-	Williamson– Hall
FWHM	-	Full width at half maximum
3D	-	Three-dimensional
EDX, EDS	-	Energy dispersive x-ray spectroscopy
TN	-	True negative
VIM	-	Variation of information metric
Spiro-OMeTAD	-	2,2',7,7'-Tetrakis[N,N-di(4-methoxyphenyl)amino]-9,9'-spirobifluorene
PEDOT:PSS	-	poly(3,4-ethylenedioxythiophene) polystyrene sulfonate
NiO	-	Nickel oxide
ZnO	-	Zinc oxide
ITO	-	Indium-doped tin oxide
CuSCN	-	Copper(I) thiocyanate
CuI	-	Copper(I) iodide
Cu ₂ O	-	Copper(I) oxide
CuO	-	Copper(II) oxide
CoO	-	Cobalt(II) oxide
MAPbI ₃ , CH ₃ NH ₃ PbI ₃	-	Methylammonium lead iodide
Ag	-	Silver
SO ₂	-	Sulfur dioxide
NO _x	-	Nitrogen oxides
CdTe	-	Cadmium telluride
CIGS	-	Copper indium gallium diselenide
GaAs	-	Gallium arsenide
CaTiO ₃	-	Calcium titanate
Pb(II)	-	Lead(II)
Sn(II)	-	Tin(II)
I ⁻	-	Iodide
Br ⁻	-	Bromine
Cl ⁻	-	Chloride
Al	-	Aluminum
PbI ₂	-	Lead(II) iodide
MAI	-	Methylammonium iodide

TiO ₂	-	Titanium dioxide
In ₂ O ₃	-	Indium oxide
SnO ₂	-	Tin(IV) oxide
WO _x	-	Tungsten oxide
CNTs	-	Carbon nanotubes
MACl	-	Methylammonium chloride
AZO	-	Al into sol-gel ZnO
rGO	-	Reduced graphene oxide
FACs	-	Formamidinium mixed with cesium cations
MgO	-	Magnesium oxide
PCBM	-	Phenyl-C61-butyric acid methyl ester
GQDs	-	Graphene quantum dots
Li-TFSI	-	Lithium bis(trifluoromethane)sulfonimide
TBP	-	4-tert-butyl pyridine
P3HT	-	poly(3-hexylthiophene-2,5-diyl
PTAA	-	Poly(triarylamine)
LED	-	Light-emitting diodes
CuS	-	Copper sulfide
CuInS ₂	-	Copper indium sulfide
CuZnSnS ₄ , CZTS	-	Copper zinc tin sulfide
MoO _x	-	Molybdenum trioxide
VBM	-	Valence band maximum
MEA	-	Monoethanolamine
KOH	-	Potassium hydroxide
DEA	-	Diethanolamine
NaOH	-	Sodium hydroxide
PVA	-	Polyvinyl alcohol
H ₃ O ⁺	-	Hydronium ion
OH	-	Hydroxide
PEG	-	Polyethylene Glycol
PVP	-	Polyvinylpyrrolidone
NiCl ₂	-	Nickel chloride
FESEM	-	Field emission electron microscope
GO	-	Graphene oxide
FTO	-	Fluorine-doped tin oxide

Ni(OH) ₂	-	Nickel hydroxide
Cs	-	Cesium
BCP	-	Bathocuproine
C ₆₀	-	Buckminsterfullerene
ZrAcac	-	Zirconium acetylacetone
DMF	-	N,N dimethylformamide
DMSO	-	Dimethyl sulfoxide
EC	-	Ethyl cellulose
C ₁₀ H ₁₈ O	-	α -terpineol
IPA, C ₃ H ₈ O	-	Isopropyl alcohol
C ₂ H ₅ OH	-	Ethanol
DI	-	Deionized water
CoO	-	Cobalt(II) oxide
Ni(CH ₃ COO) ₂ .4(H ₂ O)	-	Nickel acetate tetrahydrate
SiC	-	Silicon carbide
GaN	-	Gallium nitride
MOSFET	-	Metal–oxide semiconductor field-effect transistor
Pt	-	Platinum
Ni	-	Nickel
C	-	Carbon
O	-	Oxygen
ACQ	-	Aggregation caused quenching
AIE	-	Aggregation-induced emission
DLE	-	Deep-level-emission
Vo	-	Oxygen vacancies
Sb-	-	Antimony
Bi-	-	Bismuth
Ge-	-	Germanium
Cu-	-	Copper
SILAR	-	Successive ionic layer adsorption and reaction
KBr	-	Potassium Bromide
CO ₂	-	Carbon dioxide
H ₂ O	-	Water